JACS
JOURNAL OF THE AMERICAN CHEMICAL SOCIETY
pubs.acs.org/JACS
Article

Mechanistic Connections between CO_2 and CO Hydrogenation on Dispersed Ruthenium Nanoparticles

Haefa Mansour and Enrique Iglesia*

Cite This: J. Am. Chem. Soc. 2021, 143, 11582−11594
Read Online

ABSTRACT: Catalytic routes for upgrading CO_2 to CO and hydrocarbons have been studied for decades, and yet the mechanistic details and structure−function relationships that control catalytic performance have remained unresolved. This study elucidates the elementary steps that mediate these reactions and examines them within the context of the established mechanism for CO hydrogenation to resolve the persistent discrepancies and to demonstrate inextricable links between CO_2 and CO hydrogenation on dispersed Ru nanoparticles (6−12 nm mean diameter, 573 K). The formation of CH_4 from both CO_2−H_2 and CO−H_2 reactants requires the cleavage of strong C≡O bonds in chemisorbed CO, formed as an intermediate in both reactions, via hydrogen-assisted activation pathways. The C═O bonds in CO_2 are cleaved via direct interactions with exposed Ru atoms in elementary steps that are shown to be facile by fast isotopic scrambling of $C^{16}O_2$−$C^{18}O_2$−H_2 mixtures. Such CO_2 activation steps form bound CO molecules and O atoms; the latter are removed via H-addition steps to form H_2O. The kinetic hurdles in forming CH_4 from CO_2 do not reflect the inertness of C═O bonds in CO_2 but instead reflect the intermediate formation of CO molecules, which contain stronger C≡O bonds than CO_2 and are present at near-saturation coverages during CO_2 and CO hydrogenation catalysis. The conclusions presented herein are informed by a combination of spectroscopic, isotopic, and kinetic measurements coupled with the use of analysis methods that account for strong rate inhibition by chemisorbed CO. Such methods enable the assessment of intrinsic reaction rates and are essential to accurately determine the effects of nanoparticle structure and composition on reactivity and selectivity for CO_2−H_2 reactions.

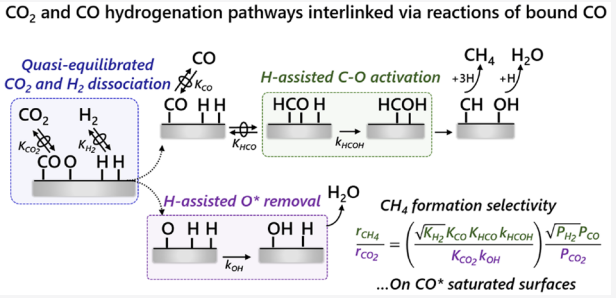

1. INTRODUCTION

The thermodynamic stability of CO_2 molecules and their rising atmospheric levels render the upgrading of CO_2 to higher-value products a challenging but important catalytic endeavor. Metal nanoparticles, and even single metal atoms, have been shown to activate C═O bonds in CO_2, thus providing direct catalytic routes for its hydrogenation to more valuable C_1 intermediates or products, such as CO, CH_4, and CH_3OH, at modest temperatures (443−673 K).[1−4] The thermodynamics of CH_4 and CO formation from CO_2 and H_2 (methanation and reverse water-gas shift reactions, respectively) are far more favorable than CH_3OH synthesis reactions, which give low equilibrium yields at the temperatures required for practical rates (ΔG_{rxn} = +75 kJ mol^{-1} for CH_3OH synthesis, −40 kJ mol^{-1} for methanation, +14 kJ mol^{-1} for reverse water-gas shift; per mole CO_2, 673 K). The significance of methanation and reverse water-gas shift in CO_2 utilization efforts and the promising catalytic routes for such reactions have attracted substantial attention in the recent literature.[1−10]

Previous attempts at relating catalytic properties to CO_2 hydrogenation rates and selectivities (to CO and CH_4) have led to persistent mechanistic questions that remain unresolved.[1,3,11] These enduring controversies include the connections between the elementary steps that form CO and CH_4 during CO_2−H_2 catalysis on transition metal surfaces and which ones among those steps limit rates and selectivities. Ru nanoparticles are among the most active and selective catalysts for CO_2 methanation, leading to their preeminence as state-of-the art catalysts in mechanistic studies of CO_2 hydrogenation.[5−7,10,12,13] Several recent studies on Ru-based catalysts concur that CO and CH_4 formation pathways occur on the same catalytic surfaces and that they are linked through the intervening formation of chemisorbed CO (CO*, where * denotes bound species).[6,10,12] Steady-state and transient infrared spectroscopy and temperature-programmed desorption data[14−16] show that surfaces are significantly covered by CO* as most abundant reactive intermediates during CO and CO_2 hydrogenation reactions. The minimum-energy paths that activate the first C═O bond in CO_2 and the second C≡O bond (in CO), which differ markedly in strength (bond-

Received: April 25, 2021
Published: July 21, 2021

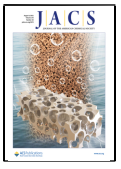

https://doi.org/10.1021/jacs.1c04298
J. Am. Chem. Soc. 2021, 143, 11582−11594

dissociation enthalpies of 532 kJ mol^{-1} for OC═O and 1075 kJ mol^{-1} for C≡O in the gas phase, 298 K),[17] and their respective kinetic relevance on working catalytic surfaces, however, remain unclear. Many studies[12,14,16,18−21] suggest that CO* is formed along with a bound O atom (O*) as a product of direct dissociation of a C═O bond in CO_2. H-assisted CO_2 activation pathways that form bound COOH or HCOO intermediates, which undergo subsequent C−O cleavage to form OH* and CO*, have also been previously proposed, but density functional theory (DFT)-derived barriers for such routes are higher than those for direct CO_2 activation routes on oxophilic metals commonly used for CO_2 methanation (e.g., Ru, Rh, Ni, and Co).[22,23] The kinetic hurdles involved in direct CO_2 activation pathways are the subject of enduring debate, however, with proposals for the kinetically relevant step that include CO* desorption[12] and H_2O formation.[23] The pathway involved in the activation of CO* (to ultimately form CH_4) on Ru surfaces also remains uncertain; some studies propose direct activation of C≡O to form C* and O*,[24−26] while others suggest H-assisted pathways with CH_xO* formation[6] or dissociation[12] as kinetically-relevant steps.

In this study, we combine kinetic and isotopic measurements over a broad pressure range during CO_2−H_2 reactions and in situ infrared spectroscopy during CO_2−CO−H_2 reactions with theoretical treatments of C≡O activation from previous studies[27−29] in order to assess the identity and kinetic relevance of bound intermediates and elementary steps involved in forming CO, CH_4, and H_2O from CO_2−H_2 reactants on Ru nanoparticles dispersed on inert SiO_2 supports. In doing so, we present an integral method of kinetic analysis that is essential to examine CO_2 hydrogenation and other CO-forming reactions and to accurately assess reaction selectivities, which are often obscured by the ubiquitous strong inhibition by the CO molecules formed during such reactions. The infrared spectra measured during CO_2−H_2 and CO−H_2 catalysis on Ru/SiO_2 are essentially identical and show high CO* coverages that are a single-valued function of CO pressure (0.75−1 ML CO*, 0.05−0.85 kPa CO), irrespective of whether CO is used as a reactant (CO−H_2 reactions) or formed as a product (CO_2−H_2 reactions). The kinetic trends observed for CO_2−H_2 reactions are also remarkably similar to those for CO−H_2 reactions when prevalent CO pressures, which increase in the axial direction as CO is formed along the catalyst bed, are rigorously accounted for using integral analysis methods for plug-flow reactors. The results of this analysis show that CH_4 formation rates during CO_2−H_2 reactions are proportional to H_2 pressure and described by the same rate equation as previously reported for CO−H_2 reactions,[28,30,31] providing compelling evidence for the inextricable links between CO_2 and CO reactions with H_2.

CH_4 formation from both CO_2−H_2 and CO−H_2 reactants involves kinetically relevant H-assisted activation of the strong C≡O bonds in CO* species that prevail as dense adlayers on Ru surfaces during steady-state catalysis. The weaker C═O bonds in CO_2, in contrast, cleave via direct dissociation on exposed vacant sites (*) in quasi-equilibrated steps that form CO* and O* as products. CO_2 conversion rates are limited by the removal of O* via sequential H-addition steps that ultimately form H_2O and complete the catalytic cycle. These mechanistic connections between CO_2 and CO hydrogenation reactions bring together the mechanistic details of CO_2 hydrogenation routes derived from this study with the knowledge gained from systematic studies of CO−H_2 reactions on Ru and other metals in the context of Fischer-Tropsch synthesis reactions.

2. EXPERIMENTAL METHODS

2.1. Catalyst Synthesis and Characterization. Ru/SiO_2 catalysts were prepared using ligand-assisted dispersion methods via incipient wetness impregnation of SiO_2 powders with aqueous $Ru(NO)(NO_3)_3$ and triethanolamine (TEA) solutions.[32] SiO_2 (Davisil 646, 300 m^2 g^{-1}) was treated in flowing dry air (Praxair, 99.99%, 10.0 cm^3 g^{-1} s^{-1}) by heating to 898 K at 0.033 K s^{-1} and holding for 5 h before impregnation. The impregnating solution, containing $Ru(NO)(NO_3)_3$ (Alfa Aesar, 31 wt % Ru) and TEA (Sigma-Aldrich, 99%) in deionized H_2O (1:5 Ru/TEA molar ratio), was added to the treated SiO_2 support in amounts corresponding to its pore volume for each of the two catalyst samples. The impregnated solids (0.5 wt % Ru for one sample and 5 wt % Ru for the other) were treated in ambient air overnight at 373 K, then heated in flowing dry air (Praxair, 99.99%, 10.0 cm^3 g^{-1} s^{-1}) to 548 K at 0.0167 K s^{-1}, held for 4 h, and cooled to ambient temperature. Samples were then heated to 723 K at 0.0167 K s^{-1} in flowing 10% H_2/He (Praxair, 99.999%, 0.5 cm^3 g^{-1} s^{-1}) and held for 3 h; these processes led to the formation of Ru nanoparticles, which were passivated by contact with flowing 2% O_2/He (Praxair, 99.99%, 1 cm^3 g^{-1} s^{-1}) at ambient temperature before exposure to air.

The dispersion of the Ru nanoparticles, defined as the ratio of surface to total Ru atoms, was determined from the total uptakes of chemisorbed hydrogen measured volumetrically at 373 K, by assuming a 1:1 $H/Ru_{surface}$ adsorption stoichiometry. Prior to the H_2 uptake measurements, catalyst samples were treated at 623 K in flowing H_2 (Praxair, 99.999%, 1 cm^3 g^{-1} s^{-1}) for 1 h, evacuated (<10^{-2} mbar) for 1 h using a dual-stage rotary vane pump (Leybold, Trivac D2.5E) and a turbomolecular drag pump (Pfeiffer Vacuum, TMU 071 P), and then cooled to 373 K. H_2 was dosed stepwise into the adsorption chamber (0.02 to 80 kPa H_2, 373 K), and total uptakes were determined from the constant uptake values measured above ∼25 kPa H_2. The adsorption chamber volume was determined by dosing He into the evacuated chamber using the same process as for H_2. Surface-averaged particle diameters were determined from dispersion values by assuming spherical nanoparticles and the atomic density of bulk Ru metal.

2.2. Measurements of Infrared Spectra during CO_2−H_2, CO−H_2, and CO_2−CO−H_2 Reactions. Infrared (IR) spectra were measured by averaging 64 scans (400−4000 cm^{-1} range, 2 cm^{-1} resolution) during CO_2−H_2 and CO−H_2 reactions using a Thermo Nicolet 8700 FT-IR spectrometer equipped with a liquid N_2-cooled MCT detector. Ru/SiO_2 samples were pressed into self-supporting catalyst wafers (10 mg cm^{-2}) and placed within a quartz in situ flow cell fitted with KBr windows. The wafer temperature was measured using a K-type thermocouple (Omega) positioned within a thermowell in contact with the radial edge of the wafer; the cell temperature was maintained by using an electronic temperature controller (Watlow, Series 982) and resistive heating (ARi Industries, BXX09B38-4T).

These wafers were treated in flowing 10% H_2/He (Praxair, 99.999%, 30 cm^3 g^{-1} s^{-1}) by heating to 698 K at 0.083 K s^{-1} and holding for 1 h before cooling to 573 K. Background spectra were measured in flowing H_2/He before exposing the wafers to flowing CO_2 (Praxair, 99.995%) or CO (Praxair, 99.999%, 1.0% CO/He); these background spectra, along with spectral contributions from gaseous CO and H_2O, were subtracted from all spectra measured during catalysis to extract the contributions from bound species. The components evident from these infrared bands were extracted from measured spectra using Gaussian−Lorentzian mixed functions.[33] The reactant and product concentrations in the effluent stream were measured using a gas chromatograph (Agilent, 7980A) equipped with a capillary column (HP-PLOT Q, 30 m × 0.53 mm × 40 μm), methanizer (Activated Research Company, Polyarc), and a flame ionization detector (FID).

2.3. CO_2 Hydrogenation Reactivity and Selectivity Measurements. Ru/SiO_2 catalysts were diluted with additional SiO_2 (Davisil 646, 300 m^2 g^{-1}) that was treated as described in section 2.1; these catalyst mixtures were pelleted and sieved to retain 150−250 μm aggregates and diluted further with quartz powder (Sigma-Aldrich, no. 204358) in order to eliminate heat and mass transfer corruptions.[34] Further details about the elimination of transport artifacts are provided in section S1.3 of the Supporting Information. The mixtures were placed within a packed-bed tubular reactor (quartz, 4 mm i.d.) with

https://doi.org/10.1021/jacs.1c04298
J. Am. Chem. Soc. 2021, 143, 11582−11594

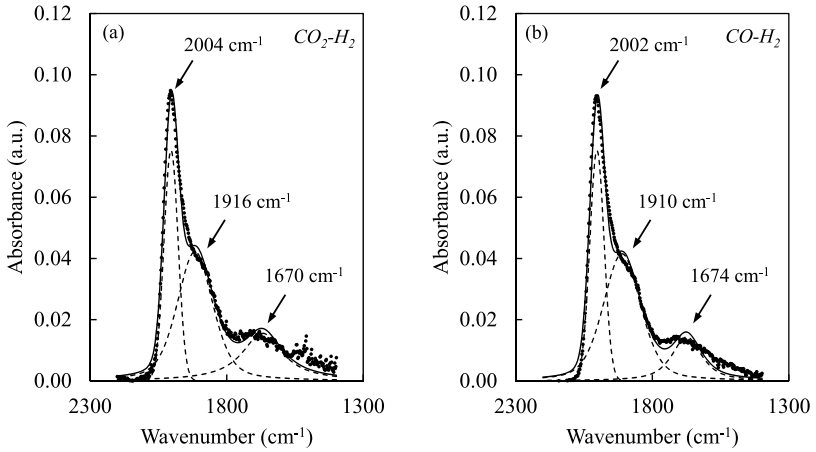

Figure 1. In situ infrared spectra and deconvoluted bands during steady state (a) CO_2−H_2 (573 K, 5 kPa CO_2, 8 kPa H_2, balance He) and (b) CO−H_2 (573 K, 0.2 kPa CO, 8 kPa H_2, balance He) reactions on 0.5 wt % Ru/SiO_2 (10 mg Ru/SiO_2 cm^{-1} wafer).

plug-flow hydrodynamics that was held within a three-zone resistively-heated furnace equipped with electronic controllers (Watlow, Series 988). Bed temperatures were measured with a K-type thermocouple in contact with the outer tube wall.

Inlet molar flow rates were metered using electronic mass flow controllers (Parker, 201) at ambient pressure. Ru/SiO_2 samples were treated in flowing 10% H_2/He (Praxair, 99.999%, 200 cm^3 g^{-1} s^{-1}) by heating to 698 K at 0.083 K s^{-1} and holding for 1 h before cooling to reaction temperature (573−673 K). The composition of the inlet stream was set by mixing CO_2 (Praxair, 99.995%), H_2 (Praxair, 99.999%), and He (Praxair, 99.999%) as balance to achieve CO_2 pressures between 1 and 16 kPa and H_2 pressures between 2 and 16 kPa. Concentrations of all species in the inlet and effluent streams were measured by gas chromatography (Agilent GC, 6890) using a packed column (Porapak Q, 2.74 m length, 2 mm i.d.) and a thermal conductivity detector (TCD). CO, CH_4, and H_2O were the main products detected; trace quantities of other hydrocarbons (C_2H_4 and C_2H_6) in the effluent stream were also detected (C_2/CH_4 molar ratio <0.005 across all conditions). CO and CH_4 formation rates (r_{CO} and r_{CH_4}, respectively) represent the net rates of formation for each product, and CO_2 consumption rates (r_{CO_2}) represent the rate of conversion of CO_2 to CO and CH_4. All reported rates are normalized by the number of surface Ru atoms, as determined from H_2 uptakes at 373 K (section 2.1).

2.4. $C^{16}O_2$−$C^{18}O_2$ Isotopic-Exchange Measurements during CO_2−H_2 Reactions. $C^{16}O_2$−$C^{18}O_2$−H_2 mixtures were used as reactants in a recirculating batch reactor (135 cm^3 volume) at ambient pressure on Ru/SiO_2 samples that were prepared and treated as described in section 2.1. $C^{16}O_2$ (Praxair, 99.995%), $C^{18}O_2$ (Sigma-Aldrich, 95 atom % ^{18}O), H_2 (Praxair, 99.999%), and He (Praxair, 99.999%) were introduced into the batch reactor after evacuation and circulated using a graphite-gear pump (Micropump, model GA-V23.CFS.C) for 1 ks before contacting the catalyst bed that was held at 573 K.

Gas aliquots were extracted from the recirculating stream using a sampling valve (VICI, six-port) and transferred to a gas chromatograph (Agilent, 7980A) equipped with a capillary column (HP-PLOT Q, 30 m × 0.53 mm × 40 μm), a methanizer (Activated Research Company, Polyarc), and a flame ionization detector (FID). Chemical and isotopic speciation were determined using a mass-selective detector (Agilent, 5975C) after separation by capillary chromatography (HP-1, 50 m × 0.32 mm × 1.05 μm). Values of the molar fraction of CO_2 present as the $C^{16}O^{18}O$ isotopologue (denoted as μ) were measured relative to the values expected from isotopic equilibration (μ_{equil}, binomial distribution) to give the approach to equilibrium for ^{16}O−^{18}O isotopic exchange (η_{exch}) as follows,

$$\eta_{exch} = \frac{\mu}{\mu_{equil}} \quad (1)$$

$$\mu_{equil} = 2\lambda(1 - \lambda) \quad (2)$$

where λ is the fractional content of ^{16}O in all CO_2 present in the system.

3. RESULTS AND DISCUSSION

3.1. In Situ Infrared Spectra during CO_2−H_2, CO−H_2, and CO_2−CO−H_2 Reactions. The identity and coverages of bound species and their involvement as intermediates were assessed from infrared spectra measured during CO_2 and CO hydrogenation on Ru/SiO_2 catalysts with concurrent measurements of rates. The infrared spectra obtained during CO_2 hydrogenation (573 K; 5 kPa CO_2, 8 kPa H_2, balance He) on 0.5 wt % Ru/SiO_2 (Figure 1a) showed three bands corresponding to the C−O stretching modes of bound CO (CO*) at 2004, 1916, and 1670 cm^{-1}. Backdonation of electron density from the metal into the CO antibonding $2\pi^*$ orbital leads to the elongation and weakening of C−O bonds and to the observed shift to lower frequencies relative to that of gaseous CO (2140 cm^{-1}).[35] This effect becomes stronger as CO binds to larger metal ensembles, thus causing distinct spectral features for CO bound to metal ensembles of varying sizes; the three bands at 2004, 1916, and 1670 cm^{-1} (Figure 1a) correspond to CO* bound atop one Ru atom, bridging two Ru atoms, and interacting with several Ru atoms, respectively.[36] Infrared features for bound formate (HCOO*) species, previously reported during CO_2−H_2 reactions on Ru nanoparticles dispersed on Al_2O_3[24] or TiO_2[25] supports, were not detected on Ru/SiO_2; such bound HCOO* species have been shown to act as mere spectators interacting with acid−base pairs on such supports[12,18] and are not present at detectable coverages on SiO_2 supports or Ru nanoparticles.

Figure 1b shows the infrared spectrum during reactions of CO−H_2 on 0.5 wt % Ru/SiO_2 at 573 K. In parts a and b of Figure 1, the samples are in contact with the same CO and H_2 pressures (0.2 kPa CO, measured at the infrared cell outlet and equivalent to the pressure at the center of the wafer for the well-mixed cell compartment; 8 kPa H_2); they differ only in the presence or substantial absence of CO_2 (5 kPa, Figure 1a; <0.02 kPa, Figure 1b). The C−O bands are essentially identical, in frequency and intensity, for these two spectra, indicative of bound CO species that are similar, in type and coverage, whether CO is used as a

https://doi.org/10.1021/jacs.1c04298
J. Am. Chem. Soc. 2021, 143, 11582−11594

reactant or formed as a product in CO_2–H_2 reactions. CO pressures were varied from 0.05 to 0.9 kPa CO during CO–H_2 reactions, and the resulting spectra are shown in Figure 2. The

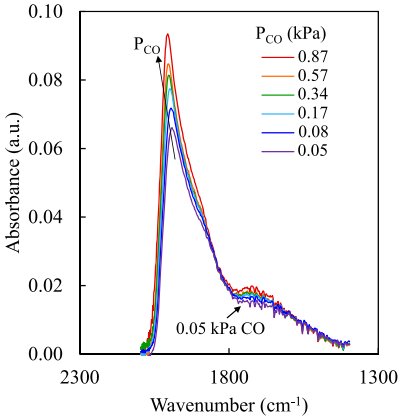

Figure 2. In situ infrared spectra during steady-state CO–H_2 reactions (573 K, 0.05–0.9 kPa CO, 4 kPa H_2, balance He) on 0.5 wt % Ru/SiO_2.

combined integrated intensities of the three CO* bands increased by a factor of 1.3 as the CO pressure increased from 0.05 to 0.9 kPa, indicative of significant coverages of CO*, which form adlayers that reach near-saturation levels at ~1 kPa CO. The CO* bands shift to higher frequencies as CO pressure increases, as previously reported,[28,37] because of weaker backdonation from the metal into $2\pi^*$ CO orbitals with increasing CO* coverage and also because of the stronger dipole–dipole coupling among CO* species at higher coverages.[37,38]

Figure 3 shows fractional CO* coverages, determined from the combined integrated intensities of the three CO* bands,

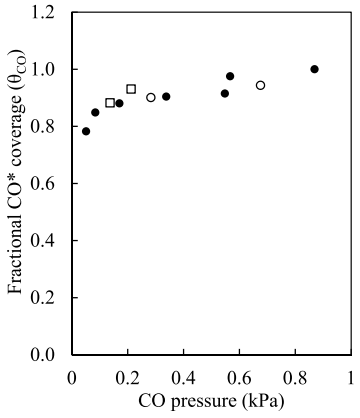

Figure 3. Fractional CO* coverages as a function of CO pressure during steady-state CO–H_2 (●), CO–CO_2–H_2 (○), and CO_2–H_2 (□) reactions determined from integrated IR bands on 0.5 wt % Ru/SiO_2. Fractional CO* coverages calculated by normalizing the integrated intensities of the three CO* bands to the maximum integrated intensities (at 0.9 kPa CO).

during steady-state reactions of CO–H_2, CO–CO_2–H_2, and CO_2–H_2 mixture at 0.05–0.9 kPa CO pressures; such coverage estimates are normalized by the maximum integrated band intensities observed in this study (at 0.9 kPa CO), which represent saturation CO* coverages at 573 K.[28] The CO* coverages derived from the spectra during CO_2–H_2 and CO–H_2 catalysis (shown at one condition in Figure 1 and at several other conditions in Figure 3) are a single-valued function of the CO pressure. CO_2–H_2 reactions (Figures 1a and 3) form CO* via surface-mediated steps that ultimately desorb CO, thus leading to CO* surface coverages that must equal (at equilibrium) or exceed (if desorption steps are not equilibrated) those expected at equilibrium with the contacting CO(g) pressure. During CO–H_2 reactions, CO* forms via adsorption of CO(g) (Figures 1b and 3); CO* coverages must therefore be equal to or below those in equilibrium with the contacting CO(g) pressure. Yet, CO* coverages are similar during CO–H_2, CO_2–H_2, and CO–CO_2–H_2 at each CO pressure, even at prevalent CO pressures that lead to submonolayer CO* coverages, indicative of CO adsorption–desorption quasi-equilibrium during both CO_2–H_2 and CO–H_2 reactions.

CO adsorption–desorption quasi-equilibrium requires that these steps occur in each direction at rates much higher than those for CO_2 or CO hydrogenation reactions. CO* desorption rates are given by

$$r_{CO^*\text{desorption}} = \frac{k_B T}{h} e^{\left(\frac{\Delta S^{\ddagger}_{des}}{k_B}\right)} e^{\left(-\frac{\Delta H^{\ddagger}_{des}}{k_B T}\right)} [CO^*] \quad (3)$$

where k_B and h are the Boltzmann and Planck constants, T is the absolute temperature, and $\Delta S^{\ddagger}_{des}$ and $\Delta H^{\ddagger}_{des}$ are the entropy and enthalpy components of the CO* desorption free energy barriers, respectively. A lower limit for CO* desorption rates can be estimated by assuming that desorption leads to the gain of one mode of translation and that desorption barriers equal the heat of CO adsorption (+100 kJ mol^{-1} on 7 nm Ru nanoparticles at 0.6 ML CO*);[39] these assumptions lead to desorption rates of ~10^7 s^{-1} at 573 K. CO_2 hydrogenation rates are much smaller (<1 s^{-1}; 0.6–0.9 ML CO*; 573 K, 1–25 kPa CO_2, 1–16 kPa H_2), consistent with quasi-equilibrated CO adsorption–desorption during CO_2–H_2 reactions. CO adsorption–desorption steps have also been shown to be fast and quasi-equilibrated during CO–H_2 reactions on Ru,[27,28,30] Fe,[40,41] and Co.[40,42,43]

The quasi-equilibrium of CO adsorption–desorption steps renders the CH_4 molecules that form before CO* desorption as kinetically indistinguishable from those that form after CO* desorbs and readsorbs. Measured CO formation rates ($r_{CO,net}$) during CO_2–H_2 reactions reflect the net rate of CO formation, as given by

$$r_{CO,net} = r_{CO^*,des}(1 - \eta) \quad (4)$$

$$\eta = \frac{[CO][*]}{K_{CO^*,des}[CO^*]} \quad (5)$$

Here, $r_{CO^*,des}$ represents the forward CO* desorption rate, η represents the approach to adsorption-desorption equilibrium, and $K_{CO^*,des}$ represents the equilibrium constant of the CO* adsorption-desorption step. As CO* desorption approaches equilibrium ($\eta \rightarrow 1$), $r_{CO,net}$ becomes much smaller than $r_{CO^*,des}$ and measured CO formation rates no longer reflect the intrinsic dynamics of CO* desorption–readsorption steps. Measured CO formation rates instead reflect the rate at which CO(g), present at pressures in equilibrium with the prevalent CO* coverages, leaves the reactor in the effluent stream. The quasi-equilibrated nature of CO* desorption precludes the use of CO formation rates as a meaningful "counter" of the rate at which CO forms via the elementary steps that activate CO_2 at Ru surfaces. CO_2 consumption rates (r_{CO_2}) and CH_4 formation rates (r_{CH_4}), the difference of which gives CO formation rates

https://doi.org/10.1021/jacs.1c04298
J. Am. Chem. Soc. 2021, 143, 11582–11594

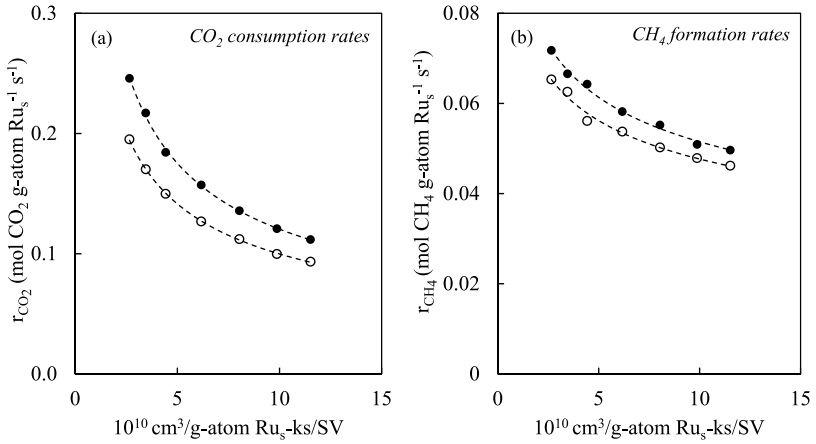

Figure 4. Effect of residence time (SV^{-1}; SV denotes space velocity) on (a) CO_2 consumption rates and (b) CH_4 formation rates on 0.5 wt % Ru/SiO_2 [573 K; 16 kPa CO_2, 8 kPa H_2, balance He (●); 8 kPa CO_2, 8 kPa H_2, balance He (○)]. Dashed lines are used to guide the eye.

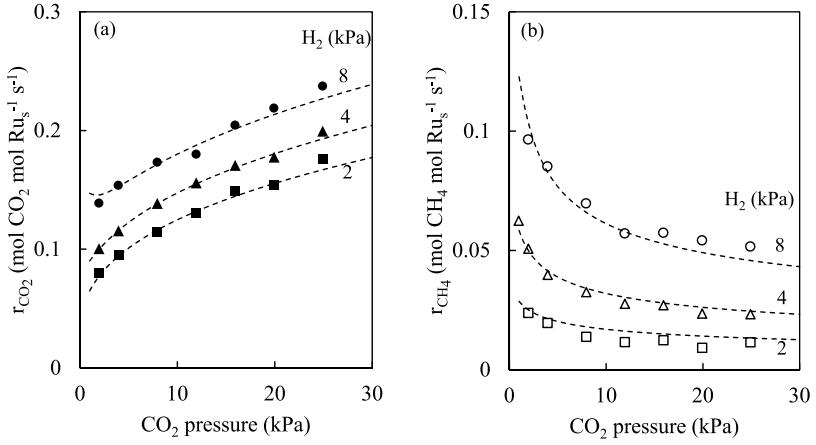

Figure 5. CO_2 pressure effects on (a) CO_2 consumption rates and (b) CH_4 formation rates on 0.5 wt % Ru/SiO_2 (573 K; 1−25 kPa CO_2, 2−8 kPa H_2, balance He; 3.5×10^5 $cm^3/(g{\cdot}atom\ Ru_s{\cdot}ks)/SV$; CO_2 conversion 0.006−0.12). Dashed curves represent the best regression fits of the rate data to the integrated forms of eqs 8 and 9.

(r_{CO}), instead represent the simplest measures of reactivity for these catalytic events and are used to describe the intrinsic dynamics of CO_2−H_2 reactions in the following sections.

3.2. Effects of Residence Time and Reactant Pressures on CO_2 Consumption Rates and CH_4 Formation Rates. CO_2 consumption and CH_4 formation rates (r_{CO_2} and r_{CH_4}, respectively; normalized per exposed Ru atom, determined from H_2 chemisorption uptakes) were measured in a packed-bed reactor with plug-flow hydrodynamics at 573 K at different CO_2 and H_2 pressures (1−25 kPa CO_2, 2−16 kPa H_2). Measured rates were unaffected by the mean diameter of the Ru/SiO_2 porous aggregates (165 vs 215 μm) or by dilution of such aggregates with quartz (bed dilution ratio = 20−70), thus ruling out any corruptions of measured rates by intra-aggregate concentration gradients or bed-temperature gradients (section S1.3 in the Supporting Information). Forward CO_2 consumption rates ($r_{CO_2,f}$) were obtained by correcting measured rates ($r_{CO_2,net}$) for the approach to equilibrium (η_1),

$$\eta_1 = \frac{P_{CO}P_{H_2O}}{P_{CO_2}P_{H_2}}\frac{1}{K_{EQ,1}} \quad (6)$$

$$r_{CO_2,net} = r_{CO_2,f}(1 - \eta_1) \quad (7)$$

where $K_{EQ,1}$ is the equilibrium constant for CO_2−H_2 conversion to CO and H_2O as products (reverse water-gas shift reaction) at the reaction temperature (η_1 = 0.005−0.1 at 573 K in these experiments). CO_2 conversion to CH_4 and H_2O is far from equilibrium ($\eta < 10^{-6}$), thus requiring no corrections.

CO_2 consumption and CH_4 formation rates from CO_2−H_2 reactants on Ru/SiO_2 decrease with increasing residence time (ratio of catalyst mass to flow rate), even at CO_2 and H_2 conversions below 10% (Figure 4; 573 K; 8−16 kPa CO_2, 8 kPa H_2), consistent with rates inhibited by one or more of the products. H_2O added to the inlet stream at pressures (1 kPa H_2O) ~10-fold larger than indigenously formed did not lead to detectable decreases in rates (Figure S2), indicating that CO is the inhibiting product (linear average CO pressure from 0.04 to 0.09 kPa; Figure 4). Such effects are consistent with the high CO* coverages evident from the infrared spectra measured during catalysis (0.05−1 kPa CO; Figures 1−3). CO* binds to the Ru surface atoms required for the kinetically-relevant elementary steps that limit CO_2 consumption and CH_4 formation turnovers. Such inhibition effects are ubiquitous in CO hydrogenation studies, leading to rate equations that contain denominator terms that depend on CO pressures on Ru[27,28,30] and Co[40] catalysts and to the large fractional coverages of CO* (θ_{CO}) evident from CO* infrared bands, even at very low CO pressures (e.g., 0.6, at 0.03 kPa CO; 598 K).[28]

https://doi.org/10.1021/jacs.1c04298
J. Am. Chem. Soc. 2021, 143, 11582−11594

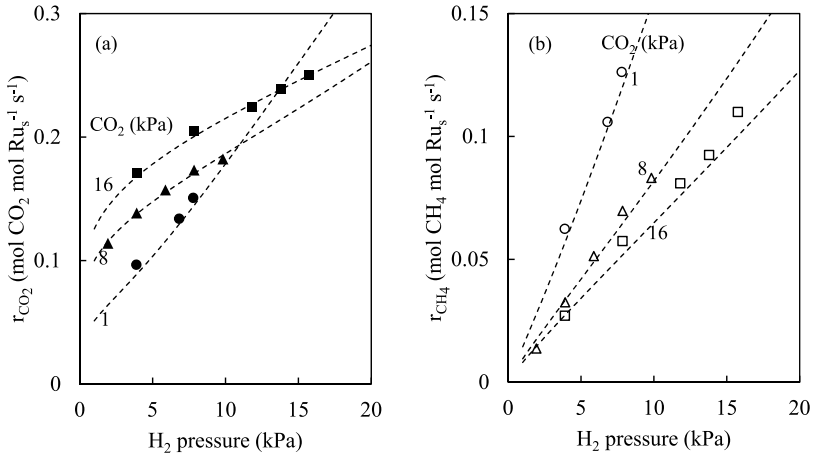

Figure 6. H_2 pressure effects on (a) CO_2 consumption rates and (b) CH_4 formation rates on 0.5% wt. Ru/SiO_2 (573 K; 1−16 kPa CO_2, 1−16 kPa H_2, balance He; 3.5×10^5 $cm^3/(g{\cdot}atom\ Ru_s{\cdot}ks)$/SV; CO_2 conversion 0.006−0.12). Dashed curves represent the best regression fits of the rate data to the integrated forms of eqs 8 and 9.

Axial gradients in the concentration of CO products, combined with strong inhibition of rates by CO, lead to significant changes in rates along the catalyst bed as conversion occurs, even at relatively low CO_2 conversions (<10%). Consequently, differential reactor formalisms, which rely upon the assumption of constant rates along the bed, cannot accurately describe intrinsic kinetic trends, which require instead integral reactor methods of analysis that rigorously account for axial CO concentration profiles. This also requires the simultaneous regression of rate data for both CO_2 consumption and CH_4 formation to a set of coupled rate equations in integral form (details provided in section S2.1 in the Supporting Information) because the prevalent CO pressures depend on the rates of both reactions, as they form and consume CO along the catalyst bed. Such methods and a systematic examination of plausible sequences of elementary steps and their respective rate equations have not been previously used in mechanistic and kinetic inquiries into CO_2 hydrogenation reactions to our knowledge. These analysis methods are used next in order to describe the effects of CO_2 and H_2 pressures on intrinsic CH_4 formation rates and CO_2 consumption rates in terms of mechanism-based rate equations.

CH_4 formation rates and (forward) CO_2 consumption rates from CO_2−H_2 reactants are influenced by CO_2 (Figure 5) and H_2 (Figure 6) pressures at 573 K on Ru/SiO_2. CO_2 consumption rates increase monotonically with CO_2 and H_2 pressure (Figures 5a and 6a) for rates obtained at the same residence time; CH_4 formation rates, in contrast, depend inversely on CO_2 pressure (Figure 5b) and almost linearly on H_2 pressure (Figure 6b). These observed kinetic trends reflect the consequences not only of the intended changes in CO_2 and H_2 pressures but also of the different prevalent CO pressures present along the bed for each condition.

The rate data in Figures 5 and 6 (and the additional data in section 3.5) were regressed to various sets of mechanism-based rate equations for CO_2 consumption and CH_4 formation (enumerated in Table S2) using integral methods. These rate equations reflect a range of potential mechanisms and kinetically relevant steps mediated by transition states that are bound to either one or two Ru surface sites, including unassisted CO_2 activation (on bare Ru atoms), hydrogen-assisted CO_2 activation, and O* removal steps as kinetically-relevant steps for CO_2 consumption and hydrogen-assisted CO activation[27,28] as the kinetically relevant step in CH_4 formation. The observed kinetic trends are described most accurately by the following rate equations for CO_2 consumption rates and CH_4 formation rates,

$$r_{CO_2} = \frac{\alpha \frac{P_{CO_2}\sqrt{P_{H_2}}}{P_{CO}}}{1 + \beta P_{CO}} \tag{8}$$

$$r_{CH_4} = \frac{\gamma P_{H_2} P_{CO}}{(1 + \beta P_{CO})^2} \tag{9}$$

where P_i represents the pressure of species i and α, β, and γ represent lumped kinetic and thermodynamic parameters. The dashed curves in Figures 5 and 6 represent the regressed fit to the functional forms of eqs 8 and 9 with lumped parameters derived from integral reactor methods (section S2.1 in the Supporting Information) and all rate data (parity plots for all data in section 3.5). The unity terms in the denominators of eqs 8 and 9 become negligible when βP_{CO} is $\gg$1; bed-averaged values obtained for βP_{CO} ranged from 0.9 to 8.5, resulting in cross-correlation between the numerator and denominator terms at some of the conditions used in this study (section S2.4 in the Supporting Information). The functional forms of these rate equations are examined next in the context of the elementary steps that interconnect bound intermediates and transition states; such a mechanistic analysis assigns chemical significance to the α, β, and γ parameters in eqs 8 and 9 for CO_2 conversion (section 3.3) and CH_4 formation (section 3.4).

3.3. Elementary Steps Involved in CO_2 Consumption Reactions during CO_2−H_2 Reactions. The ability of eqs 8 and 9, which contain identical terms in their denominators, to accurately describe both CO_2 consumption and CH_4 formation rates demonstrates that these reactions, sometimes treated as independent routes on different active sites,[44] occur instead via interlinked steps on the same catalytic surfaces. The two terms (1 and βP_{CO}; eqs 8 and 9) are ubiquitous in CO hydrogenation rate equations[27,28,30] and reflect the relative concentrations of bare surface atoms (*) and bound CO* in Langmuirian kinetic treatments. Such precise origins have been recently questioned[28] based on discrepancies between the values of equilibrium constants for binding of molecular CO (K_{CO}) derived from regressions of rate data at high CO pressures (>1 kPa) and those determined from in situ infrared spectra and

https://doi.org/10.1021/jacs.1c04298
J. Am. Chem. Soc. 2021, 143, 11582−11594

theoretical treatments. These discrepancies, caused by significant intermolecular repulsions within dense CO* adlayers, preclude accurate descriptions using Langmuirian treatments at the high CO pressures typical of CO methanation reactions (1−100 kPa CO) but not at the low CO pressures prevalent in this study (<0.1 kPa CO). In fact, CO hydrogenation rates at CO* coverages between 0.5 and 0.9 ML (0.01−0.1 kPa CO, 573 K) were accurately described by Langmuirian models, which gave values of K_{CO} consistent with those determined independently from infrared spectra.[28] The two terms in the denominators of the CO_2 consumption and CH_4 formation rate equations (eqs 8 and 9) likewise reflect * and CO* species, the relative concentrations of which are determined by K_{CO} (represented by β). The values of β obtained from the regression of rate data for CO_2−H_2 reactions are consistent with those obtained from kinetic data and in situ infrared spectra for CO−H_2 reactions,[28] as shown in section 3.5 for two catalysts with different mean nanoparticle diameters.

The absence of H_2-dependent terms in the denominators of the rate equations (eqs 8 and 9) indicates that coverages of H_2-derived species are negligible at the conditions used in this study. Previous kinetics studies of CO−H_2 reactions have similarly found that the rate equations that describe such reactions do not contain H_2-dependent terms in their denominators.[30,40,43] DFT treatments have shown that Ru surfaces can bind H atoms at interstitial spaces present within CO* adlayers.[28,31] Chemisorbed H atoms (denoted as H′) do not displace CO* species bound in atop configuration but reside instead at three-fold hollow sites on Ru surfaces containing significant CO* coverages.[31]

The numerator term in the equation that describes CO_2 consumption rates (eq 8, section 3.2) reflects the composition of the transition state (TS) that mediates the kinetically-relevant step for CO_2 consumption during CO_2−H_2 reactions. It suggests a kinetically-relevant TS structure that contains one O atom and one H atom, a heuristic analysis confirmed by the kinetic treatment below. Chemisorbed O atoms (O*) and CO* form as products of CO_2 activation on vicinal Ru atom pairs when it occurs without assistance by H_2-derived species. Such CO_2 activation steps have been suggested by DFT studies on Ru,[23] Rh,[21−23] and Ni[22,23] surfaces. The CO* formed can desorb and readsorb, thus establishing equilibrium with the contacting CO(g) phase, as shown in section 3.1. The O* species must ultimately react via sequential H-addition steps to form OH* and H_2O* (Scheme 1); O* can also react with CO*, thus reversing its formation step before reacting with H′ to form H_2O. When this reverse step is fast relative to the step that forms H_2O, unassisted CO_2 activation steps become quasi-equilibrated. Taken together with the quasi-equilibrated nature of CO* adsorption−desorption, this would lead to O* coverages set by the following equation,

$$\frac{[O^*]}{[^*]} = \left(\frac{K_{CO_2}}{K_{CO}}\right) \times \left(\frac{P_{CO_2}}{P_{CO}}\right) \tag{10}$$

where K_{CO_2} is the equilibrium constant for CO_2 dissociation to O* and CO*. CO*-saturated Ru surfaces bind both O* and H′ at three-fold sites, but O atom binding requires displacement of CO*,[45] whereas H atom binding occurs at interstitial sites within CO* adlayers.[31] Consequently, the kinetically-relevant reaction of O* with H′ to form OH* may involve a single Ru atom, which, together with the prevalence of CO* and * as the most abundant bound species, gives the rate equation for CO_2 consumption (derivation in section S2.2 in the Supporting Information):

$$r_{CO_2} = \frac{\left(\frac{K_{CO_2}\sqrt{K_{H_2}}k_{OH}}{K_{CO}}\right) \times \left(\frac{P_{CO_2}\sqrt{P_{H_2}}}{P_{CO}}\right)}{1 + K_{CO}P_{CO}} \tag{11}$$

This equation has the functional form of eq 8 with α (in eq 8) given by $K_{CO_2}\sqrt{K_{H_2}}k_{OH}K_{CO}^{-1}$ and β (in eqs 8 and 9) corresponding to K_{CO}. The form of eq 8 is consistent with CO_2 hydrogenation pathways that form O* and CO* as intermediates, but not with H-assisted CO_2 activation pathways because such pathways directly form OH* and CO*[22,46] and thus do not involve any elementary steps that are mediated by TS structures containing only O and H atoms.

The sequence of elementary steps in Scheme 1 requires quasi-equilibrated CO_2 activation steps to give the functional form of the rate equation that accurately describes measured CO_2 consumption rates (eq 8). This occurs when reactions of O* with CO* are much faster than those with H′ to form OH* (and ultimately H_2O). Previous experimental and DFT studies of CO hydrogenation on Fe, Co, and Ru surfaces have shown that O*, formed in infrequent unassisted CO activation during CO−H_2 reactions, reacts preferentially with CO* (to form CO_2) instead of H′ (to form H_2O).[40,47] Such a preference is consistent with the prevalence of CO_2 over H_2O as the predominant oxygen-rejection route, as well as with the prevalent, very large (CO*)/(H′) ratios on working surfaces.

The extent of equilibration of CO_2 activation steps during CO_2−H_2 reactions was examined by measuring the CO_2 isotopologues formed during $C^{16}O_2$−$C^{18}O_2$−H_2 reactions with equimolar amounts of $C^{16}O_2$ and $C^{18}O_2$. Figure 7 shows the relative concentrations of $C^{16}O_2$, $C^{18}O_2$, and $C^{16}O^{18}O$ at a fractional CO_2 conversion of 0.02, a value within the range of conversions used in flow experiments in section 3.2 (0.01−0.05); the resulting distribution of isotopologues from equimolar mixtures of $C^{16}O_2$ and $C^{18}O_2$ is binomial. The CO_2 fraction present as the mixed $C^{16}O^{18}O$ isotopologue (0.49) leads to a value for the approach to equilibrium of $C^{16}O_2$−$C^{18}O_2$ isotopic exchange (η_{exch}, calculated as described in section 2.4) of 0.99 at conditions where the approach to equilibrium of CO_2-consuming reactions is insignificant (<0.05). These results confirm that CO_2 activation steps are quasi-equilibrated during CO_2−H_2 reactions, consistent with the form of the CO_2 consumption rate equation (eq 8) and with the expectations

Scheme 1. Elementary Steps and Associated Thermodynamic and Kinetic Constants for CO_2−H_2 Reactions that Form CO and H_2O on Ru Surfaces[a]

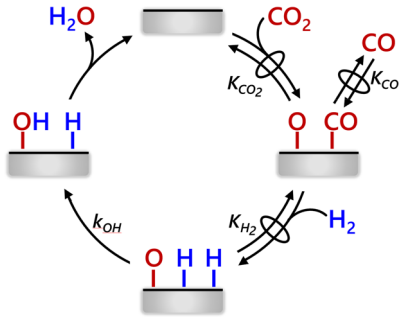

[a]Arrows with superimposed ovals denote quasi-equilibrated steps. *K* denotes thermodynamic constants, and *k* denotes kinetic constants.

https://doi.org/10.1021/jacs.1c04298
J. Am. Chem. Soc. 2021, 143, 11582−11594

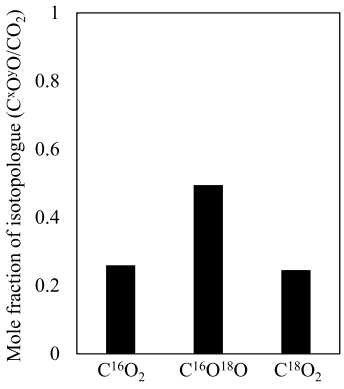

Figure 7. CO_2 isotopologue distribution during $C^{16}O_2$–$C^{18}O_2$–H_2 reactions (0.02 CO_2 conversion; 3.6 kPa $C^{16}O_2$, 3.4 kPa $C^{18}O_2$, 4 kPa H_2, balance He, 573 K, 7.9×10^{-10} g·atom Ru_s·ks·cm^{-3}; 0.5 wt % Ru/SiO_2). Approach to equilibrium for reverse water-gas shift and methanation reactions <0.05.

of faster O*–CO* reactions than O*–H′ reactions set by previous CO hydrogenation studies.[40,47] Next, we combine these CO_2 conversion elementary steps with those for CH_4 formation in order to determine the nature of the kinetically-relevant TS for both reactions.

3.4. Elementary Steps Involved in the Formation of CH_4 from CO_2–H_2 and CO–H_2 Reactants. The numerator in the CH_4 formation rate equation (eq 9) reflects the stoichiometry of the transition state that mediates the kinetically-relevant step for CH_4 formation during CO_2–H_2 reactions. CO, but not CO_2, appears in this numerator, indicative of CH_4 molecules that form through an intermediate present at coverages that reflect the contacting CO(g) pressure and that are insensitive to the concurrent presence or pressure of CO_2. Such results are in agreement with infrared spectra (section 3.1) that show CO* to be the most abundant surface intermediate and to be present at coverages in quasi-equilibrium with CO(g) and independent of CO_2 pressure. The involvement of CO* as an intermediate in CH_4 formation for both CO–H_2 and CO_2–H_2 reactions leads to the same rate equation for CH_4 formation from CO_2–H_2 (eq 9) and CO–H_2[28,31] reactants on Ru nanoparticles. CO* forms from CO_2 via unassisted CO_2 activation (section 3.3) and its coverage reaches quasi-equilibrium with the contacting CO(g) pressure along the bed. CH_4 forms via H-assisted activation of CO* via the same intermediates and transition states as when CO is present at the inlet in CO–H_2 reactions. The H_2 dependence in the numerator of eq 9 thus reflects the prevalence of H-assisted routes for kinetically-relevant CO* activation, as shown for CO–H_2 reactions on Ru over a much broader CO pressure range (0.001–100 kPa CO, 518–598 K)[28] and also for Co[29,40,48,49] and Fe catalysts.[40]

Scheme 2 depicts the sequence of elementary steps that accounts for the formation of CH_4 and H_2O as products of either CO_2–H_2 or CO–H_2 reactants. Quasi-equilibrated adsorption of CO and H_2 is followed by the quasi-equilibrated formation of formyl species (HC*O*) via H-addition to CO*. The kinetically relevant step involves the additional weakening of C–O bonds via another H-addition (to HC*O*), which forms hydroxymethylene species (HC*O*H) that cleave in a fast subsequent step to form CH* and OH*. These latter species react with additional H atoms in fast subsequent steps to form CH_4 and H_2O as the products of CO methanation. The CH_x species also act as monomers and initiators for chain growth in the Fischer-Tropsch synthesis.[40]

Scheme 2. Elementary Steps and Their Thermodynamic and Kinetic Parameters for CO–H_2 Reactions That Form CH_4 and H_2O on Ru Surfaces[a]

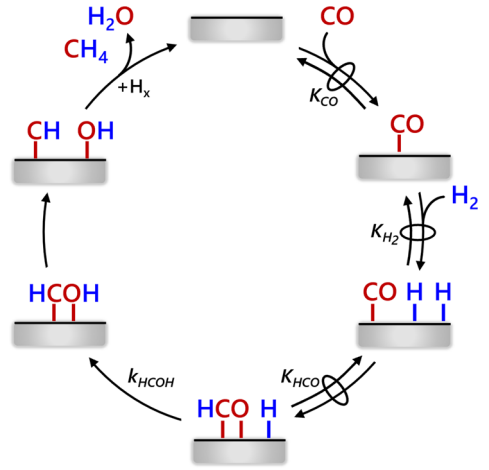

[a]Arrows with superimposed ovals denote quasi-equilibrated steps. *K* denotes thermodynamic constants, and *k* denotes kinetic constants.

Such hydrogen-assisted C–O activation routes form OH* instead of O* (formed in unassisted direct C–O activation), consistent with the prevalence of H_2O over CO_2 as the predominant O-rejection path on Ru and Co surfaces[28,40] and with DFT-derived barriers for various plausible CH_4 formation pathways for CO hydrogenation on Ru nanoparticles. DFT-derived energies on Ru_{201} nanoparticles at high CO* coverages (1.55 CO*/Ru, maximum CO* coverage that maintains atop CO* binding on terraces) have shown that hydrogen-assisted CO activation barriers (165 kJ mol^{-1}) on (111) terraces are significantly smaller than those for unassisted direct CO* dissociation routes, which occur on bare Ru sites and form C* and O* as products (322–356 kJ mol^{-1}).[27]

The hydrogen-assisted pathway depicted in Scheme 2, taken together with the assumptions of CO* and * as the most abundant surface intermediates, leads to an equation for CH_4 formation rates with the functional form of eq 9 (derivation provided in section S2.3 in the Supporting Information):

$$r_{CH_4} = \frac{K_{H_2} K_{CO} K_{HCO} k_{HCOH} P_{H_2} P_{CO}}{(1 + K_{CO} P_{CO})^2} \quad (12)$$

This equation assigns chemical significance to γ in eq 9.

Scheme 3 depicts the complete sequence of elementary steps involved in the formation of CO, CH_4, and H_2O from CO_2–H_2 mixtures. Quasi-equilibrated CO_2 and H_2 dissociation steps form CO*, which subsequently desorbs molecularly, and O* and H′, which combine to form OH* and ultimately H_2O, thus completing a reverse water-gas shift catalytic turnover. CO* also undergoes H-addition steps before dissociation to form CH* and OH* fragments, which are hydrogenated to form CH_4 and H_2O, thus completing a methanation catalytic turnover. The next section explores the consequences of this mechanism in determining the selectivity to CH_4 in CO_2–H_2 reactions.

3.5. Consequences of Mechanism and Ru Particle Size for Selectivity of CO_2–H_2 Reactions. The mechanism described in the preceding sections and depicted in Scheme 3

https://doi.org/10.1021/jacs.1c04298
J. Am. Chem. Soc. 2021, 143, 11582–11594

Scheme 3. Elementary Steps and Associated Thermodynamic and Kinetic Constants for CO_2−H_2 Reactions That Form CO, CH_4, and H_2O on Ru Surfaces[a]

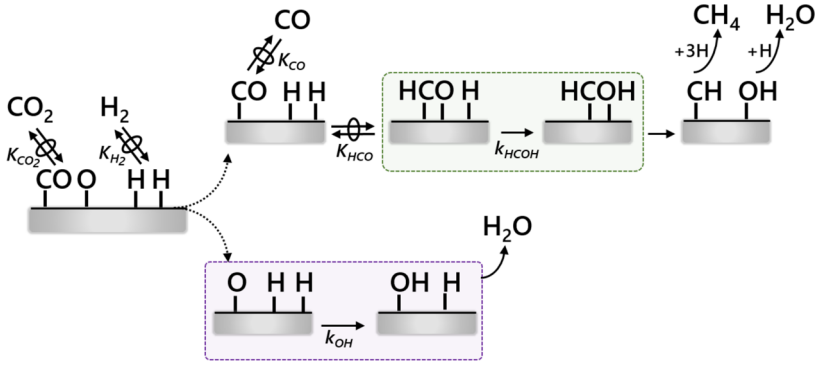

[a]Arrows with superimposed ovals denote quasi-equilibrated steps, K denotes thermodynamic constants, and k denotes kinetic constants. Shaded boxes indicate the rate-determining steps for CO_2 consumption and CH_4 formation.

gives a measure of CH_4 selectivity, defined here as the ratio of CH_4 rates to CO_2 consumption rates:

$$\frac{r_{CH_4}}{r_{CO_2}} = \left(\frac{\sqrt{K_{H_2}}K_{CO}{}^2K_{HCO}k_{HCOH}}{K_{CO_2}k_{OH}}\right) \times \frac{\sqrt{P_{H_2}}P_{CO}{}^2}{P_{CO_2}(1 + K_{CO}P_{CO})} \tag{13}$$

This equation reflects the combination of eqs 11 and 12 and relates such ratios to the prevalent pressures of reactants and products when surfaces are nearly saturated with CO* ($K_{CO}P_{CO} \gg 1$):

$$\frac{r_{CH_4}}{r_{CO_2}} = \chi\frac{\sqrt{P_{H_2}}P_{CO}}{P_{CO_2}} \tag{14}$$

$$\chi = \frac{\sqrt{K_{H_2}}K_{CO}K_{HCO}k_{HCOH}}{K_{CO_2}k_{OH}} \tag{15}$$

The value of χ represents a grouping of the relevant rate and equilibrium constants for the steps depicted in Scheme 3. Figure 8 shows measured CH_4 selectivities during CO_2−H_2 catalysis as a function of the expression in eq 14; the resulting relationship is nearly linear when average CO pressures are >0.04 kPa (closed circles), conditions that lead to high CO* coverages, in agreement with eqs 14 and 15 and indicative of the involvement and kinetic relevance of the proposed elementary steps (Scheme 3).

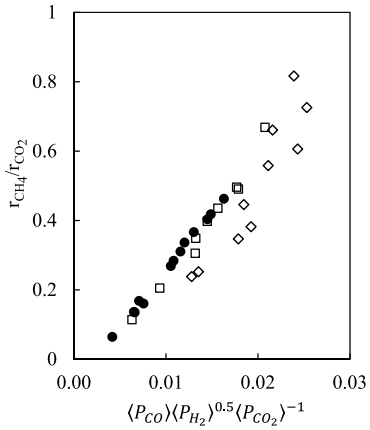

Figure 8. Effect of $\langle P_{CO}\rangle\langle P_{H_2}\rangle^{0.5}\langle P_{CO_2}\rangle^{-1}$ pressure ratios on apparent CH_4 selectivities for $\langle P_{CO}\rangle$ between 0.008 and 0.02 kPa (◇), $\langle P_{CO}\rangle$ between 0.02 and 0.04 kPa (□), and $\langle P_{CO}\rangle$ between 0.04 and 0.08 kPa (●) [573 K; 1−25 kPa CO_2, 1−16 kPa H_2, balance He; 0.5 wt % Ru/SiO_2)]. $\langle P_i\rangle$ denotes the linear average of P_i at the reactor inlet and outlet.

Previous studies have addressed the effects of nanoparticle size on CH_4 selectivity,[1,5,44,50] with conclusions still subject to significant debate.[5,51] Many reports show that small nanoparticles (<3 nm) and single atoms are highly selective for CH_4 formation;[51−54] other studies show instead that small nanoparticles and single atoms exclusively form CO and H_2O from CO_2−H_2 reactants[50,55] and that CH_4 selectivities become higher as nanoparticle size increases.[44,56] These contradictions and other differences in reported selectivities are attributed to different and nonuniform nanoparticle structures among samples and to structural motifs formed in reaction environments.[5,44,50] The mechanism-based integral reactor treatment shown here to be essential in the analysis of CO_2 hydrogenation rates and selectivities indicates that such contradictions also reflect differences in conversion and prevalent CO pressures among such studies. In the absence of such treatments, selectivity comparisons among catalysts become uninformative and often misleading, even when measured at low reactant conversions.

The value of χ in eq 15 represents the intrinsic measure of selectivity that must be used to compare catalysts. The tenets of transition-state theory[57] impose quasi-equilibrium between reactants and activated TS complexes, which gives the relationship between the kinetically-relevant transition states and their relevant precursors in the form of the following (nonelementary) reactions:

$$CO_2(g) - CO(g) + \tfrac{1}{2}H_2(g) + * \rightleftharpoons O^*\text{-}H^{\ddagger} \tag{16}$$

$$CO(g) + H_2(g) + 2^* \rightleftharpoons HC^*O^*\text{-}H^{\ddagger} \tag{17}$$

The Gibbs free energy of formation of each TS from its gaseous precursors likewise determines the groupings of rate and equilibrium constants in the numerators of eqs 11 and 12 ($K_{CO_2}\sqrt{K_{H_2}}k_{OH}K_{CO}{}^{-1}$ and $K_{H_2}K_{CO}K_{HCO}k_{HCOH}$, respectively),

$$\frac{K_{CO_2}\sqrt{K_{H_2}}k_{OH}}{K_{CO}} = \frac{k_BT}{h}\,e^{\left(-\frac{G_{O^*-H^{\ddagger}}+G_{CO}-G_{CO_2}-\frac{1}{2}G_{H_2}}{k_BT}\right)} \tag{18}$$

https://doi.org/10.1021/jacs.1c04298
J. Am. Chem. Soc. 2021, 143, 11582−11594

Table 1. Effects of Mean Ru Nanoparticle Size on Rate Parameters for CO_2-H_2 Reactions on Ru/SiO_2 Catalysts

mean Ru nanoparticle size (nm)	χ^a ($kPa^{-0.5}$)	$K_{CO}{}^{a,b}$ (kPa^{-1})	$K_{H_2}K_{CO}K_{HCO}k_{HCOH}{}^{a,b}$ (kPa^{-2} s^{-1})	$K_{CO_2}\sqrt{(K_{H_2})k_{OH}K_{CO}}{}^{-1a,b}$ ($kPa^{-0.5}$ s^{-1})
6[c]	24 ± 4	113 ± 5	8.0 ± 0.5	(2.9 ± 0.5) × 10^{-3}
11[d]	21 ± 4	59 ± 3	12.3 ± 1.3	(9.7 ± 1.5) × 10^{-3}

[a]At 573 K; 1−25 kPa CO_2, 1−16 kPa H_2, balance He. [b]Errors represent the 95% confidence intervals of the parameters obtained using bootstrapping methods.[58] [c]For 0.5 wt % Ru/SiO_2 catalysts. [d]For 5 wt % Ru/SiO_2 catalysts.

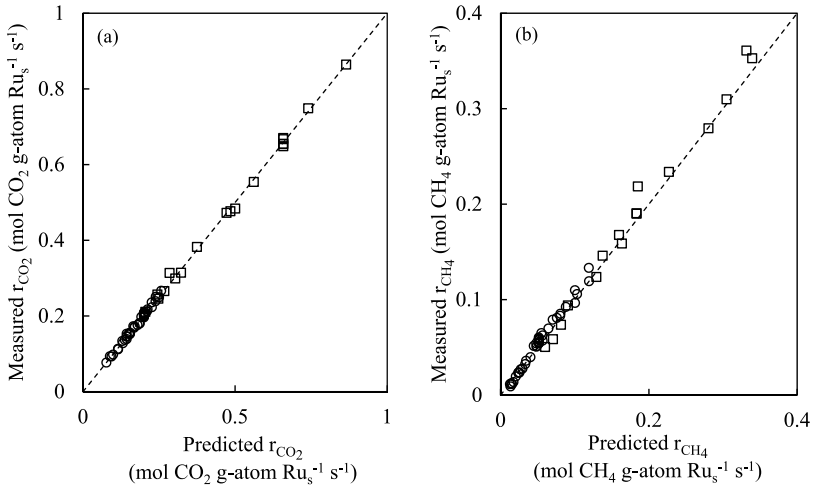

Figure 9. Parity plots for (a) CO_2 consumption rates (eq 8) and (b) CH_4 formation rates (eq 9) on 6.5 nm (○) and 11 nm (□) nanoparticles (573 K; 1−25 kPa CO_2, 1−16 kPa H_2, balance He).

$$K_{H_2}K_{CO}K_{HCO}k_{HCOH} = \frac{k_B T}{h}\, e^{\left(-\frac{G_{HC^*O^*-H^\ddagger} - G_{CO} - G_{H_2}}{k_B T}\right)} \quad (19)$$

where k_B and h are the Boltzmann and Planck constants, $G_{O^*-H^\ddagger}$ and $G_{HC^*O^*-H^\ddagger}$ are the free energies of the TS structures, and G_{CO}, G_{CO_2}, and G_{H_2} are the free energies of gaseous CO, CO_2, and H_2 molecules, respectively. The combination of eqs 18 and 19 gives the following:

$$\chi = \exp\left(\frac{\left[G_{O^*-H^\ddagger} - G_{CO_2} + G_{CO} - \frac{1}{2}G_{H_2}\right]}{RT} - \frac{[G_{HC^*O^*-H^\ddagger} - G_{CO} - G_{H_2}]}{RT} + \frac{[G_{CO^*} - G_{CO}]}{RT}\right) \quad (20)$$

Within this equation, only $G_{O^*-H^\ddagger}$, $G_{HC^*O^*-H^\ddagger}$, and G_{CO^*} (the Gibbs free energies of $O^*-H^\ddagger$, $HC^*O^*-H^\ddagger$, and CO*, respectively) depend on the binding properties of nanoparticle surfaces. As a result, any differences in χ among catalysts would indicate that the $HC^*O^*-H^\ddagger$ TS free energy differs from the combined free energies of CO* and the $O^*-H^\ddagger$ TS. The value of χ is given approximately by the slope in the linear region of Figure 8 (at high CO* coverages) and more accurately by regression of all kinetic data to the functional form of eqs 11 and 12 and the insertion of the regressed parameters into eq 15.

Table 1 shows χ values (and regressed parameters) on the catalyst used in the kinetic analysis of section 3.2 (0.5 wt % Ru/SiO_2; 6 nm mean diameter particles) together with those on a catalyst with larger nanoparticles (5 wt % Ru/SiO_2; 11 nm mean diameter). CH_4 formation and CO_2 consumption rates on both samples are accurately described by eqs 8 and 9, as shown by the agreement between the measured and predicted rates in Figure 9. The χ values for the larger and smaller nanoparticles are essentially the same (21 ± 4 $kPa^{-0.5}$ vs 24 ± 4 $kPa^{-0.5}$), suggesting that, within this range, nanoparticle size does not significantly affect product selectivities when the prevalent CO pressures for each selectivity measurement are taken into consideration.

The measured values of K_{CO} were 113 kPa^{-1} on 6 nm nanoparticles and 59 kPa^{-1} on 11 nm nanoparticles, consistent with the expected stronger binding of CO on smaller nanoparticles. Such K_{CO} values are also consistent with the results reported in previous infrared spectroscopic studies (~80 kPa^{-1} on 7.5 nm Ru nanoparticles; 0.001−0.1 kPa CO).[28] The effective CH_4 formation rate constants ($K_{H_2}K_{CO}K_{HCO}k_{HCOH}$, eq 12) from CO_2-H_2 reactants are slightly larger on 11 nm than 6 nm Ru nanoparticles (12.3 ± 1.3 kPa^{-2} s^{-1}, 11 nm; 8.0 ± 0.5 kPa^{-2} s^{-1}, 6 nm). These trends are directionally consistent with those reported for $CO-H_2$ reactions on Ru[47,59] and Co[60−63] catalysts, for which turnover rates increase with increasing nanoparticle diameter up to ~10 nm.[47,59,62] The similar effects of nanoparticle size on the rates of CH_4 formation from $CO-H_2$ and CO_2-H_2 reactants represent the natural consequence of their mechanistic connections. The trends for $CO-H_2$ reactions have been attributed to the decoration of coordinatively-unsaturated exposed atoms, which is more prevalent on smaller particles, by strongly bound CO* or by C* and O* species formed via occasional CO* dissociation events.[40,59,62,63] Direct CO* dissociation events do not contribute to measured rates, as shown by the functional form of the rate equation[28,29,40,48,49] and by their large DFT-derived barriers on both terrace and corner Ru atoms[27] (section 3.4); such infrequent events, however, render undercoordinated atoms unavailable for catalytic turnovers. This interpretation of the observed particle size effects is consistent with χ values that are insensitive to particle diameter (24 ± 4 $kPa^{-0.5}$, 6 nm; 21 ± 4 $kPa^{-0.5}$, 11 nm)

https://doi.org/10.1021/jacs.1c04298
J. Am. Chem. Soc. 2021, 143, 11582−11594

and with the higher CO_2 consumption rate constants measured on larger Ru nanoparticles ($2.9 \pm 0.5 \times 10^{-3}$ $kPa^{-0.5}$ s^{-1}, 6 nm; $9.7 \pm 1.5 \times 10^{-3}$ $kPa^{-0.5}$ s^{-1}, 11 nm).

The connection between measured reaction selectivities and prevalent CO pressures highlights an important challenge associated with empirical approaches to catalytic design without a concomitant understanding of the underlying mechanistic details. The mechanistic insights gained in this work required a type of kinetic analysis that is seldom considered in comparing turnover rates and selectivities among catalysts, but which becomes crucial for sequential reactions that form strongly-bound intermediate products. Such formalisms, both in their use of sets of coupled rate equations and integral analysis of rate data, are essential in interpreting differences among catalysts and determining the effect of nanoparticle structure and support composition on reactivity and selectivity during CO_2–H_2 reactions.

4. CONCLUSIONS

This work brings together kinetic, isotopic, and spectroscopic data measured during CO_2–H_2 reactions with the knowledge gained from decades of experimental and theoretical studies of CO–H_2 reactions to establish the identity and kinetic relevance of the elementary steps involved in CO_2 hydrogenation at moderate conditions (573 K; 1–25 kPa CO_2, 1–16 kPa H_2). In doing so, we also present kinetic analysis methods that rigorously account for inhibition by CO, which is formed and consumed along the catalyst bed, through the regression of rate data to sets of coupled rate equations in their integrated forms. Such methods are essential to accurately assess the intrinsic reactivity of metal nanoparticles for CO_2 hydrogenation (and other reactions that form strongly bound CO) and thus provide meaningful comparisons among different nanoparticle structures and compositions.

The combination of kinetic and isotopic evidence reveals that the kinetic hurdles in converting CO_2 to hydrocarbons are not imposed by the chemical inertness of CO_2, as typically claimed, but rather by the intermediate formation of CO, which contains an even stronger C≡O bond and forms near-saturated adlayers on metal surfaces at typical reaction conditions. The strong C≡O bonds in chemisorbed CO are cleaved via kinetically-relevant hydrogen-assisted activation steps, while the weaker C=O bonds in CO_2 are cleaved through quasi-equilibrated steps that involve direct interactions with exposed metal atoms to form O* and CO*. O* species are removed via sequential H-addition steps, the first of which limits CO_2 consumption turnovers. CO* species desorb and readsorb in quasi-equilibrated steps, as indicated by the similar CO* coverages obtained from infrared spectra measured during CO_2–H_2 and CO–H_2 reactions at the same prevalent CO pressures. The observations presented in this work illustrate the mechanistic connections between CO and CO_2 hydrogenation, which proceed via an identical sequence of elementary steps subsequent to the formation of CO* intermediates. These connections reward us with an ability to recycle the structure-function relationships developed in the context of Fischer-Tropsch synthesis to accelerate progress in the design of more active and selective catalysts for CO_2 hydrogenation reactions.

■ ASSOCIATED CONTENT

Supporting Information

The Supporting Information is available free of charge at https://pubs.acs.org/doi/10.1021/jacs.1c04298.

Infrared spectra at various H_2 pressures, effect of cofeeding H_2O during CO_2–H_2 reactions, testing for heat and mass transport effects, integral kinetic analysis methods, derivation of rate expressions for CO_2 consumption and CH_4 formation, and perturbation analysis to determine the extent of cross-correlation between numerator and denominator terms in the rate expressions (PDF)

■ AUTHOR INFORMATION

Corresponding Author

Enrique Iglesia − *Department of Chemical Engineering, University of California at Berkeley, Berkeley, California 94720, United States;* orcid.org/0000-0003-4109-1001; Email: iglesia@berkeley.edu

Author

Haefa Mansour − *Department of Chemical Engineering, University of California at Berkeley, Berkeley, California 94720, United States*

Complete contact information is available at: https://pubs.acs.org/10.1021/jacs.1c04298

Notes

The authors declare no competing financial interest.

■ ACKNOWLEDGMENTS

We acknowledge with thanks the financial support from the National Science Foundation for a Graduate Research Fellowship for HM, from BP p.l.c., and from the Theodore Vermeulen Chair Fund for all research activities carried out as part of this project. The authors thank Dr. Junnan Shanguang and Dr. Stephanie Kwon for their technical comments and careful proofreading of this manuscript.

■ REFERENCES

(1) Kattel, S.; Liu, P.; Chen, J. G. Tuning Selectivity of CO_2 Hydrogenation Reactions at the Metal/Oxide Interface. *J. Am. Chem. Soc.* **2017**, *139*, 9739–9754.

(2) Aziz, M. A. A.; Jalil, A. A.; Triwahyono, S.; Ahmad, A. CO_2 Methanation over Heterogeneous Catalysts: Recent Progress and Future Prospects. *Green Chem.* **2015**, *17*, 2647–2663.

(3) Jalama, K. Carbon Dioxide Hydrogenation over Nickel-, Ruthenium-, and Copper-Based Catalysts: Review of Kinetics and Mechanism. *Catal. Rev.: Sci. Eng.* **2017**, *59* (2), 95–164.

(4) Frontera, P.; Macario, A.; Ferraro, M.; Antonucci, P. L. Supported Catalysts for CO_2 Methanation: A Review. *Catalysts* **2017**, *7*, 59.

(5) Aitbekova, A.; Wu, L.; Wrasman, C. J.; Boubnov, A.; Hoffman, A. S.; Goodman, E. D.; Bare, S. R.; Cargnello, M. Low-Temperature Restructuring of CeO_2-Supported Ru Nanoparticles Determines Selectivity in CO_2 Catalytic Reduction. *J. Am. Chem. Soc.* **2018**, *140* (42), 13736–13745.

(6) Navarro-Jaén, S.; Navarro, J. C.; Bobadilla, L. F.; Centeno, M. A.; Laguna, O. H.; Odriozola, J. A. Size-Tailored Ru Nanoparticles Deposited over γ-Al_2O_3 for the CO_2 Methanation Reaction. *Appl. Surf. Sci.* **2019**, *483*, 750–761.

(7) Sakpal, T.; Lefferts, L. Structure-Dependent Activity of CeO_2 Supported Ru Catalysts for CO_2 Methanation. *J. Catal.* **2018**, *367*, 171–180.

(8) Younas, M.; Loong Kong, L.; Bashir, M. J. K.; Nadeem, H.; Shehzad, A.; Sethupathi, S. Recent Advancements, Fundamental Challenges, and Opportunities in Catalytic Methanation of CO. *Energy Fuels* **2016**, *30*, 8815–8831.

(9) Parastaev, A.; Muravev, V.; Huertas Osta, E.; van Hoof, A. J. F.; Kimpel, T. F.; Kosinov, N.; Hensen, E. J. M. Boosting CO_2

Hydrogenation via Size-Dependent Metal−Support Interactions in Cobalt/Ceria-Based Catalysts. *Nat. Catal.* **2020**, *3* (6), 526−533.
(10) Navarro-Jaén, S.; Szego, A.; Bobadilla, L. F.; Laguna, Ó. H.; Romero-Sarria, F.; Centeno, M. A.; Odriozola, J. A. Operando Spectroscopic Evidence of the Induced Effect of Residual Species in the Reaction Intermediates during CO_2 Hydrogenation over Ruthenium Nanoparticles. *ChemCatChem* **2019**, *11* (8), 2063−2068.
(11) Ye, R. P.; Ding, J.; Gong, W.; Argyle, M. D.; Zhong, Q.; Wang, Y.; Russell, C. K.; Xu, Z.; Russell, A. G.; Li, Q.; et al. CO_2 Hydrogenation to High-Value Products via Heterogeneous Catalysis. *Nat. Commun.* **2019**, *10*, 1−15.
(12) Avanesian, T.; Gusmão, G. S.; Christopher, P. Mechanism of CO_2 Reduction by H_2 on Ru(0 0 0 1) and General Selectivity Descriptors for Late-Transition Metal Catalysts. *J. Catal.* **2016**, *343*, 86−96.
(13) Falbo, L.; Martinelli, M.; Visconti, C. G.; Lietti, L.; Bassano, C.; Deiana, P. Kinetics of CO_2 Methanation on a Ru-Based Catalyst at Process Conditions Relevant for Power-to-Gas Applications. *Appl. Catal., B* **2018**, *225*, 354−363.
(14) Martin, G. A.; Primet, M.; Dalmon, J. A. Reactions of CO and CO_2 on $NiSiO_2$ above 373 K as Studied by Infrared Spectroscopic and Magnetic Methods. *J. Catal.* **1978**, *53* (3), 321−330.
(15) Fisher, I. A.; Bell, A. T. A Comparative Study of CO and CO_2 Hydrogenation over Rh/SiO_2. *J. Catal.* **1996**, *162* (1), 54−65.
(16) Falconer, J. L.; Zağli, A. E. Adsorption and Methanation of Carbon Dioxide on a Nickel/Silica Catalyst. *J. Catal.* **1980**, *62* (2), 280−285.
(17) Dean, J. A. *Lange's Handbook Of Chemistry*, 15th ed.; McGraw-Hill: New York, 1999; p 318.
(18) Eckle, S.; Anfang, H. G.; Behm, R. J. Reaction Intermediates and Side Products in the Methanation of CO and CO_2 over Supported Ru Catalysts in H_2-Rich Reformate Gases. *J. Phys. Chem. C* **2011**, *115* (4), 1361−1367.
(19) Abdel-Mageed, A. M.; Eckle, S.; Anfang, H. G.; Behm, R. J. Selective CO Methanation in CO_2-Rich H_2 Atmospheres over a Ru/Zeolite Catalyst: The Influence of Catalyst Calcination. *J. Catal.* **2013**, *298*, 148−160.
(20) Weatherbee, G. D.; Bartholomew, C. H. Hydrogenation of CO_2 on Group VIII Metals. II. Kinetics and Mechanism of CO_2 Hydrogenation on Nickel. *J. Catal.* **1982**, *77* (2), 460−472.
(21) Maestri, M.; Reuter, K. Molecular-Level Understanding of WGS and Reverse WGS Reactions on Rh through Hierarchical Multiscale Approach. *Chem. Eng. Sci.* **2012**, *74*, 296−299.
(22) Dietz, L.; Piccinin, S.; Maestri, M. Mechanistic Insights into CO_2 Activation via Reverse Water - Gas Shift on Metal Surfaces. *J. Phys. Chem. C* **2015**, *119* (9), 4959−4966.
(23) Qi, Y.; Zhu, Y.-A.; Chen, D. Mechanism Investigation and Catalyst Screening of High-Temperature Reverse Water Gas Shift Reaction. *Green Chem. Eng.* **2020**, *1* (2), 131−139.
(24) Solymosi, F.; Erdöhelyi, A.; Kocsis, M. Methanation of CO_2 on Supported Ru Catalysts. *J. Chem. Soc., Faraday Trans. 1* **1981**, *77* (5), 1003−1012.
(25) Prairie, M. R.; Renken, A.; Highfield, J. G.; Ravindranathan Thampi, K.; Grätzel, M. A Fourier Transform Infrared Spectroscopic Study of CO_2 Methanation on Supported Ruthenium. *J. Catal.* **1991**, *129* (1), 130−144.
(26) Wang, F.; Zhang, S.; Li, C.; Liu, J.; He, S.; Zhao, Y.; Yan, H.; Wei, M.; Evans, D. G.; Duan, X. Catalytic Behavior of Supported Ru Nanoparticles on the (101) and (001) Facets of Anatase TiO_2. *RSC Adv.* **2014**, *4* (21), 10834−10840.
(27) Loveless, B. T.; Buda, C.; Neurock, M.; Iglesia, E. CO Chemisorption and Dissociation at High Coverages during CO Hydrogenation on Ru Catalysts. *J. Am. Chem. Soc.* **2013**, *135* (16), 6107−6121.
(28) Liu, J.; Hibbitts, D.; Iglesia, E. Dense CO Adlayers as Enablers of CO Hydrogenation Turnovers on Ru Surfaces. *J. Am. Chem. Soc.* **2017**, *139* (34), 11789−11802.
(29) Qi, Y.; Yang, J.; Duan, X.; Zhu, Y. A.; Chen, D.; Holmen, A. Discrimination of the Mechanism of CH_4 Formation in Fischer−Tropsch Synthesis on Co Catalysts: A Combined Approach of DFT, Kinetic Isotope Effects and Kinetic Analysis. *Catal. Sci. Technol.* **2014**, *4* (10), 3534−3543.
(30) Dixit, R. S.; Tavlarides, L. L. Kinetics of the Fischer−Tropsch Synthesis. *Ind. Eng. Chem. Process Des. Dev.* **1983**, *22* (1), 1−9.
(31) Hibbitts, D.; Dybeck, E.; Lawlor, T.; Neurock, M.; Iglesia, E. Preferential Activation of CO near Hydrocarbon Chains during Fischer−Tropsch Synthesis on Ru. *J. Catal.* **2016**, *337*, 91−101.
(32) Soled, S. L.; Malek, A.; Miseo, S.; Baumgartner, J.; Kliewer, C.; Afeworki, M.; Stevens, P. A. Supported Metal Catalysts: Some Interesting New Leads in an Old Field. *Stud. Surf. Sci. Catal.* **2006**, *162*, 103−110.
(33) DeNoyer, L. K.; Dodd, J. G. Sample Characterization and Spectral Data Processing. In *Handbook of Vibrational Spectroscopy*; Chalmers, J. M., Griffiths, P. R., Eds.; John Wiley & Sons, Ltd.: 2002; p 2173.
(34) Koros, R. M.; Nowak, E. J. A Diagnostic Test of the Kinetic Regime in a Packed Bed Reactor. *Chem. Eng. Sci.* **1967**, *22* (3), 470.
(35) Crabtree, R. H. Carbonyls, Phosphines, and Substitution. In *The Organometallic Chemistry of the Transition Metals*, 6th ed.; Wiley: 2014; pp 98−133; DOI: 10.1002/9781118788301.
(36) Mojet, B. L.; Ebbesen, S. D.; Lefferts, L. Light at the Interface: The Potential of Attenuated Total Reflection Infrared Spectroscopy for Understanding Heterogeneous Catalysis in Water. *Chem. Soc. Rev.* **2010**, *39*, 4643−4655.
(37) Vanolli, F.; Heiz, U.; Schneider, W. D. Vibrational Coupling of CO Adsorbed on Monodispersed Ni11 Clusters Supported on Magnesia. *Chem. Phys. Lett.* **1997**, *277* (5−6), 527−531.
(38) Hoffmann, F. M. Infrared Reflection-Absorption Spectroscopy of Adsorbed Molecules. *Surf. Sci. Rep.* **1983**, *3* (2−3), 107−192.
(39) Eslava, J. L.; Sun, X.; Gascon, J.; Kapteijn, F.; Rodríguez-Ramos, I. Ruthenium Particle Size and Cesium Promotion Effects in Fischer−Tropsch Synthesis over High-Surface-Area Graphite Supported Catalysts. *Catal. Sci. Technol.* **2017**, *7* (5), 1235−1244.
(40) Ojeda, M.; Nabar, R.; Nilekar, A. U.; Ishikawa, A.; Mavrikakis, M.; Iglesia, E. CO Activation Pathways and the Mechanism of Fischer−Tropsch Synthesis. *J. Catal.* **2010**, *272* (2), 287−297.
(41) Van Der Laan, G. P.; Beenackers, A. A. C. M. Intrinsic Kinetics of the Gas-Solid Fischer−Tropsch and Water Gas Shift Reactions over a Precipitated Iron Catalyst. *Appl. Catal., A* **2000**, *193* (1−2), 39−53.
(42) Krishnamoorthy, S.; Tu, M.; Ojeda, M. P.; Pinna, D.; Iglesia, E. An Investigation of the Effects of Water on Rate and Selectivity for the Fischer−Tropsch Synthesis on Cobalt-Based Catalysts. *J. Catal.* **2002**, *211* (2), 422−433.
(43) Yates, I. C.; Satterfield, C. N. Intrinsic Kinetics of the Fischer−Tropsch Synthesis on a Cobalt Catalyst. *Energy Fuels* **1991**, *5* (1), 168−173.
(44) Kwak, J. H.; Kovarik, L.; Szanyi, J. CO_2 Reduction on Supported Ru/Al_2O_3 Catalysts: Cluster Size Dependence of Product Selectivity. *ACS Catal.* **2013**, *3* (11), 2449−2455.
(45) Hibbitts, D. D.; Loveless, B. T.; Neurock, M.; Iglesia, E. Mechanistic Role of Water on the Rate and Selectivity of Fischer−Tropsch Synthesis on Ruthenium Catalysts. *Angew. Chem., Int. Ed.* **2013**, *52* (47), 12273−12278.
(46) Cheng, D.; Negreiros, F. R.; Aprà, E.; Fortunelli, A. Computational Approaches to the Chemical Conversion of Carbon Dioxide. *ChemSusChem* **2013**, *6*, 944−965.
(47) Loveless, B. *C−O Bond Activation and C−C Bond Formation Paths in Catalytic CO Hydrogenation*; University of California: Berkeley, 2012.
(48) Storsæter, S.; Chen, D.; Holmen, A. Microkinetic Modelling of the Formation of C1 and C2 Products in the Fischer−Tropsch Synthesis over Cobalt Catalysts. *Surf. Sci.* **2006**, *600* (10), 2051−2063.
(49) Yang, J.; Qi, Y.; Zhu, J.; Zhu, Y. A.; Chen, D.; Holmen, A. Reaction Mechanism of CO Activation and Methane Formation on Co Fischer−Tropsch Catalyst: A Combined DFT, Transient, and Steady-State Kinetic Modeling. *J. Catal.* **2013**, *308*, 37−49.

(50) Matsubu, J. C.; Yang, V. N.; Christopher, P. Isolated Metal Active Site Concentration and Stability Control Catalytic CO_2 Reduction Selectivity. *J. Am. Chem. Soc.* **2015**, *137* (8), 3076−3084.
(51) Guo, Y.; Mei, S.; Yuan, K.; Wang, D. J.; Liu, H. C.; Yan, C. H.; Zhang, Y. W. Low-Temperature CO_2 Methanation over CeO_2-Supported Ru Single Atoms, Nanoclusters, and Nanoparticles Competitively Tuned by Strong Metal-Support Interactions and H-Spillover Effect. *ACS Catal.* **2018**, *8* (7), 6203−6215.
(52) Abe, T.; Tanizawa, M.; Watanabe, K.; Taguchi, A. CO_2 Methanation Property of Ru Nanoparticle-Loaded TiO_2 Prepared by a Polygonal Barrel-Sputtering Method. *Energy Environ. Sci.* **2009**, *2* (3), 315−321.
(53) Sharma, S.; Hu, Z.; Zhang, P.; McFarland, E. W.; Metiu, H. CO_2 Methanation on Ru-Doped Ceria. *J. Catal.* **2011**, *278* (2), 297−309.
(54) Upham, D. C.; Derk, A. R.; Sharma, S.; Metiu, H.; McFarland, E. W. CO_2 Methanation by Ru-Doped Ceria: The Role of the Oxidation State of the Surface. *Catal. Sci. Technol.* **2015**, *5* (3), 1783−1791.
(55) Millet, M. M.; Algara-Siller, G.; Wrabetz, S.; Mazheika, A.; Girgsdies, F.; Teschner, D.; Seitz, F.; Tarasov, A.; Levchenko, S. V.; Schlögl, R.; et al. Ni Single Atom Catalysts for CO_2 Activation. *J. Am. Chem. Soc.* **2019**, *141*, 2451−2461.
(56) Panagiotopoulou, P. Hydrogenation of CO_2 over Supported Noble Metal Catalysts. *Appl. Catal., A* **2017**, *542*, 63−70.
(57) Anslyn, E. V.; Dougherty, D. A. Transition State Theory (TST) and Related Topics. In *Modern Physical Organic Chemistry*; University Science Books: 2006; p 365; DOI: 10.1126/science.1256018.
(58) Freedman, D. A. Bootstrapping Regression Models. In *The Annals of Statistics*; SAGE Publications, Inc.: 2007; Vol. *9*, pp 1218−1228; DOI: 10.1214/aos/1176345638.
(59) Carballo, J. M. G.; Yang, J.; Holmen, A.; García-Rodríguez, S.; Rojas, S.; Ojeda, M.; Fierro, J. L. G. Catalytic Effects of Ruthenium Particle Size on the Fischer−Tropsch Synthesis. *J. Catal.* **2011**, *284* (1), 102−108.
(60) Den Breejen, J. P.; Radstake, P. B.; Bezemer, G. L.; Bitter, J. H.; Frøseth, V.; Holmen, A.; De Jong, K. P. On the Origin of the Cobalt Particle Size Effects in Fischer−Tropsch Catalysis. *J. Am. Chem. Soc.* **2009**, *131* (20), 7197−7203.
(61) Tuxen, A.; Carenco, S.; Chintapalli, M.; Chuang, C. H.; Escudero, C.; Pach, E.; Jiang, P.; Borondics, F.; Beberwyck, B.; Alivisatos, A. P.; et al. Size-Dependent Dissociation of Carbon Monoxide on Cobalt Nanoparticles. *J. Am. Chem. Soc.* **2013**, *135* (6), 2273−2278.
(62) Yang, J.; Tveten, E. Z.; Chen, D.; Holmen, A. Understanding the Effect of Cobalt Particle Size on Fischer−Tropsch Synthesis: Surface Species and Mechanistic Studies by SSITKA and Kinetic Isotope Effect. *Langmuir* **2010**, *26* (21), 16558−16567.
(63) Yang, J.; Frøseth, V.; Chen, D.; Holmen, A. Particle Size Effect for Cobalt Fischer−Tropsch Catalysts Based on in Situ CO Chemisorption. *Surf. Sci.* **2016**, *648*, 67−73.

https://doi.org/10.1021/jacs.1c04298
J. Am. Chem. Soc. 2021, 143, 11582−11594